Research Article | Vol. 26, No. 8 | 16 Apr 2018 | OPTICS EXPRESS 10649
Optics EXPRESS

Huygens' optical vector wave field synthesis via in-plane electric dipole metasurface

HYEONSOO PARK,[1] HANSIK YUN,[1] CHULSOO CHOI,[1] JONGWOO HONG,[1] HWI KIM,[2,*] AND BYOUNGHO LEE[1]

[1]*Inter-University Semiconductor Research Center and School of Electrical and Computer Engineering, Seoul National University, Gwanakro 1, Seoul 08826, South Korea*
[2]*Department of Electronics and Information Engineering, Korea University, Sejong-ro 2511, Sejong 30019, South Korea*
[*]*hwikim@korea.ac.kr*

Abstract: We investigate Huygens' optical vector wave field synthesis scheme for electric dipole metasurfaces with the capability of modulating in-plane polarization and complex amplitude and discuss the practical issues involved in realizing multi-modulation metasurfaces. The proposed Huygens' vector wave field synthesis scheme identifies the vector Airy disk as a synthetic unit element and creates a designed vector optical field by integrating polarization-controlled and complex-modulated Airy disks. The metasurface structure for the proposed vector field synthesis is analyzed in terms of the signal-to-noise ratio of the synthesized field distribution. The design of practical metasurface structures with true vector modulation capability is possible through the analysis of the light field modulation characteristics of various complex modulated geometric phase metasurfaces. It is shown that the regularization of meta-atoms is a key factor that needs to be considered in field synthesis, given that it is essential for a wide range of optical field synthetic applications, including holographic displays, microscopy, and optical lithography.

OCIS codes: (050.6624) Subwavelength structures; (050.1960) Diffraction theory; (070.7345) Wave propagation; (160.3918) Metamaterials; (310.6628) Subwavelength structures, nanostructures.

References and links

1. H. T. Chen, A. J. Taylor, and N. Yu, "A review of metasurfaces: physics and applications," Rep. Prog. Phys. **79**(7), 076401 (2016).
2. G. Zheng, H. Mühlenbernd, M. Kenney, G. Li, T. Zentgraf, and S. Zhang, "Metasurface holograms reaching 80% efficiency," Nat. Nanotechnol. **10**(4), 308–312 (2015).
3. J. P. Balthasar Mueller, N. A. Rubin, R. C. Devlin, B. Groever, and F. Capasso, "Metasurface polarization optics: independent phase control of arbitrary orthogonal states of polarization," Phys. Rev. Lett. **118**(11), 113901 (2017).
4. F. Yue, X. Zang, D. Wen, Z. Li, C. Zhang, H. Liu, B. D. Gerardot, W. Wang, G. Zheng, and X. Chen, "Geometric phase generated optical illusion," Sci. Rep. **7**(1), 11440 (2017).
5. D. Wen, F. Yue, C. Zhang, X. Zang, H. Liu, W. Wang, and X. Chen, "Plasmonic metasurface for optical rotation," Appl. Phys. Lett. **111**(2), 023102 (2017).
6. R. C. Devlin, M. Khorasaninejad, W. T. Chen, J. Oh, and F. Capasso, "Broadband high-efficiency dielectric metasurfaces for the visible spectrum," Proc. Natl. Acad. Sci. U.S.A. **113**(38), 10473–10478 (2016).
7. D. G. Baranov, D. A. Zuev, S. I. Lepeshov, O. V. Kotov, A. E. Krasnok, A. B. Evlyukhin, and B. N. Chichkov, "All-dielectric nanophotonics: the quest for better materials and fabrication techniques," Optica **4**(7), 814–825 (2017).
8. M. Khorasaninejad and K. B. Crozier, "Silicon nanofin grating as a miniature chirality-distinguishing beam-splitter," Nat. Commun. **5**, 5386 (2014).
9. B. Groever, W. T. Chen, and F. Capasso, "Meta-lens doublet in the visible region," Nano Lett. **17**(8), 4902–4907 (2017).
10. A. Arbabi, E. Arbabi, Y. Horie, S. M. Kamali, and A. Faraon, "Planar metasurface retroreflector," Nat. Photonics **11**(7), 415–420 (2017).
11. M. Khorasaninejad, A. Y. Zhu, C. Roques-Carmes, W. T. Chen, J. Oh, I. Mishra, R. C. Devlin, and F. Capasso, "Polarization-insensitive metalenses at visible wavelengths," Nano Lett. **16**(11), 7229–7234 (2016).
12. D. Lin, A. L. Holsteen, E. Maguid, G. Wetzstein, P. G. Kik, E. Hasman, and M. L. Brongersma, "Photonic multitasking interleaved Si nanoantenna phased array," Nano Lett. **16**(12), 7671–7676 (2016).

#325901 https://doi.org/10.1364/OE.26.010649
Journal © 2018 Received 12 Mar 2018; revised 6 Apr 2018; accepted 6 Apr 2018; published 11 Apr 2018

Optics EXPRESS

13. Z. Yue, G. Xue, J. Liu, Y. Wang, and M. Gu, "Nanometric holograms based on a topological insulator material," Nat. Commun. **8**, 15354 (2017).
14. J. D. Jackson, *Classical Electrodynamics* (Wiley, 1998).
15. M. Born and E. Wolf, *Principle of Optics* (Cambridge University, 1999).
16. X. Li, H. Ren, X. Chen, J. Liu, Q. Li, C. Li, G. Xue, J. Jia, L. Cao, A. Sahu, B. Hu, Y. Wang, G. Jin, and M. Gu, "Athermally photoreduced graphene oxides for three-dimensional holographic images," Nat. Commun. **6**(1), 6984 (2015).
17. B. Richards and E. Wolf, "Electromagnetic diffraction in optical systems I. An integral representation of the image field," Proc. R. Soc. Lond. A Math. Phys. Sci. **253**(1274), 349–357 (1959).
18. B. Richards and E. Wolf, "Electromagnetic diffraction in optical systems II. Structure of the image field in an aplanatic system," Proc. R. Soc. Lond. A Math. Phys. Sci. **253**(1274), 358–379 (1959).
19. L. Novotny and B. Hecht, *Principles of Nano-optics* (Cambridge University, 2012).
20. S. P. Anokhov, "Return to foundations of wave optics," Opt. Lett. **32**(15), 2209–2211 (2007).
21. S. Guha and G. D. Gillen, "Vector diffraction theory of refraction of light by a spherical surface," J. Opt. Soc. Am. B **24**(1), 1–8 (2007).
22. R. Kant, "An analytical solution of vector diffraction for focusing optical systems," J. Mod. Opt. **40**(2), 337–347 (1993).
23. C. J. R. Sheppard and P. Török, "Efficient calculation of electromagnetic diffraction in optical systems using a multipole expansion," J. Mod. Opt. **44**(4), 803–818 (1997).
24. A. S. Marathay and J. F. McCalmont, "Vector diffraction theory for electromagnetic waves," J. Opt. Soc. Am. A **18**(10), 2585–2593 (2001).
25. S.-Y. Lee, K. Kim, S.-J. Kim, H. Park, K.-Y. Kim, and B. Lee, "Plasmonic meta-slit: shaping and controlling near-field focus," Optica **2**(1), 6–13 (2015).
26. E.-Y. Song, S.-Y. Lee, J. Hong, K. Lee, Y. Lee, G.-Y. Lee, H. Kim, and B. Lee, "A double-lined metasurface for plasmonic complex-field generation," Laser Photonics Rev. **10**(2), 299–306 (2016).
27. J. Chen, L. Li, T. Li, and S. N. Zhu, "Indefinite plasmonic beam engineering by in-plane holography," Sci. Rep. **6**(1), 28926 (2016).
28. Y. Tsur, I. Epstein, R. Remez, and A. Arie, "Wavefront shaping of plasmonic beams by selective coupling," ACS Photonics **4**(6), 1339–1343 (2017).
29. H. Park, J. Kim, Y. Jeon, B. Lee, and H. Kim, "Regularized Huygens' plasmonic wave field synthesis using a metal-clad plasmonic waveguide array," Opt. Lett. **42**(18), 3610–3613 (2017).
30. A. V. Novitsky and D. V. Novitsky, "Negative propagation of vector Bessel beams," J. Opt. Soc. Am. A **24**(9), 2844–2849 (2007).
31. W. T. Chen, M. Khorasaninejad, A. Y. Zhu, J. Oh, R. C. Devlin, A. Zaidi, and F. Capasso, "Generation of wavelength-independent subwavelength Bessel beams using metasurfaces," Light Sci. Appl. **6**(5), e16259 (2017).
32. R. Dorn, S. Quabis, and G. Leuchs, "The focus of light—linear polarization breaks the rotational symmetry of the focal spot," J. Mod. Opt. **50**(12), 1917–1926 (2003).
33. J. W. Chon, X. Gan, and M. Gu, "Splitting of the focal spot of a high numerical-aperture objective in free space," Appl. Phys. Lett. **81**(9), 1576–1578 (2002).
34. A. April, "Bessel-Gauss beams as rigorous solutions of the Helmholtz equation," J. Opt. Soc. Am. A **28**(10), 2100–2107 (2011).
35. Q. Zhan, "Cylindrical vector beams: from mathematical concepts to applications," Adv. Opt. Photonics **1**(1), 1–57 (2009).
36. Z. Bouchal and M. Olivík, "Non-diffractive vector Bessel beams," J. Mod. Opt. **42**(8), 1555–1566 (1995).
37. F. Yue, D. Wen, J. Xin, B. D. Gerardot, J. Li, and X. Chen, "Vector vortex beam generation with a single plasmonic metasurface," ACS Photonics **3**(9), 1558–1563 (2016).
38. D. G. Hall, "Vector-beam solutions of Maxwell's wave equation," Opt. Lett. **21**(1), 9–11 (1996).
39. K. Huang, P. Shi, G. W. Cao, K. Li, X. B. Zhang, and Y. P. Li, "Vector-vortex Bessel-Gauss beams and their tightly focusing properties," Opt. Lett. **36**(6), 888–890 (2011).
40. G.-Y. Lee, G. Yoon, S.-Y. Lee, H. Yun, J. Cho, K. Lee, H. Kim, J. Rho, and B. Lee, "Complete amplitude and phase control of light using broadband holographic metasurfaces," Nanoscale **10**(9), 4237–4245 (2018).
41. M. Khorasaninejad, Z. Shi, A. Y. Zhu, W. T. Chen, V. Sanjeev, A. Zaidi, and F. Capasso, "Achromatic metalens over 60 nm bandwidth in the visible and metalens with reverse chromatic dispersion," Nano Lett. **17**(3), 1819–1824 (2017).
42. F. Aieta, M. A. Kats, P. Genevet, and F. Capasso, "Multiwavelength achromatic metasurfaces by dispersive phase compensation," Science **347**(6228), 1342–1345 (2015).
43. E. Arbabi, A. Arbabi, S. M. Kamali, Y. Horie, and A. Faraon, "High efficiency double-wavelength dielectric metasurface lenses with dichroic birefringent meta-atoms," Opt. Express **24**(16), 18468–18477 (2016).

1. Introduction

Recent advances in metasurface research have led to the possibility of optical wave modulation with the eventual goal of near full controllability of the wavefront. Metasurface technology now offers the hope that the simultaneous and independent modulation of the phase, amplitude, and polarization of optical waves can be achieved on a single metasurface [1–7]. Metasurfaces are conventionally designed and fabricated in the form of thin metallic and dielectric composite patterns for practical applications [8–11], but various metasurface structures based on novel materials such as graphene and topological insulators have been proposed to expand the range of possible applications [12, 13].

Metasurface holograms are generated by metasurface-based diffractive optical elements (DOEs), each of which is characterized by a high numerical aperture (NA), high spatial frequency components, and an extremely thin structure. According to Huygens' principle, a DOE can be considered an array of elementary point light sources with specific phase and amplitude modulation values. A DOE sets optical boundary conditions that can produce a designed optical field distribution in the half-infinite free space from the DOE. A vector field metasurface hologram based on Huygens' principle can then be defined by a DOE that includes polarization, amplitude, and phase in the degree of controllability, and takes vector dipoles with a modulated amplitude and phase as an elementary point light source, i.e. meta-atoms. According to the Mie scattering theory and Babinet's principle, ultra-small dielectric rods and metallic rods can be regarded as electric dipole sources, and a subwavelength-sized slit on metallic film can serve as a magnetic dipole source under the illumination of an optical plane wave [14, 15]. The Huygens-Fresnel principle and the vector diffraction theory of light state that the boundary condition in the scattering plane can be replaced by the distribution of continuous surface magnetic and electric dipole moments, and the diffraction field is constructed from the radiation field of the dipole sources [14–24].

In this paper, we investigate Huygens' optical vector field synthesis using in-plane polarized electric dipole sources and related signal-to-noise ratio issues. In particular, based on the premise of three-dimensionally radiating regularized point-like electric-dipole meta-atoms, vector field synthesis and corresponding metasurface design problem are discussed. In Huygens' field synthesis scheme, the non-paraxiality of the elementary meta-atoms, which causes a metasurface to generate a highly non-paraxial vector wavefront of wide spatial bandwidth over the paraxial regime, needs to be accounted for. Recent work on plasmonic field synthesis [25–28] has demonstrated that the irregular scattering patterns of meta-atoms can cause a considerable disparity between the generated plasmonic field and the targeted field that has a wide spatial bandwidth [25, 26, 29] and a metal-clad waveguide array has been proposed to enable the precise regularization of the irregular scattering patterns of meta-atoms [29].

This paper is organized as follows. In Section 2, the flat-surface arrangement of in-plane electric dipole sources to generate an elementary linear-polarized Airy disk is described and a method for generating a target field by superposing elementary Airy disks is proposed. Numerical simulations demonstrate that the synthesis of an arbitrary vector field can be successfully achieved using the proposed method, and the residual field that includes cross-polarized field components is suppressed with a precisely constructed in-plane electric dipole distribution. In Section 3, numerical results for the generation of circularly polarized holograms are presented to illustrate that the regularization of the meta-atoms improves the signal-to-noise ratio for optical field synthesis. Finally, concluding remarks are provided in Section 4.

2. Vector field synthesis based on a linearly polarized Airy disk unit using an in-plane electric dipole metasurface

As depicted in Fig. 1(a), an electric dipole metasurface (EDM) can be formed from the arrangement of subwavelength-size dielectric rods on a flat substrate. Assuming that the dielectric meta-atoms are not so close to each other that their mutual interaction is negligible [1–11], we can consider the total scattering field for an EDM to be the linear superposition of the scattering fields of the individual meta-atoms in free space. Here, we argue that an EDM that has meta-atoms with arbitrary in-plane electric dipole moments can generate an arbitrary

Optics EXPRESS

vector field at a specified output plane. The design problem, schematically illustrated in Fig. 1(b), centers around determining the in-plane vector field distribution on the metasurface plane to generate a precise linear-polarized Airy disk pattern on the specific output plane, $z = z_0$.

An x-polarized Airy disk is defined as the in-plane electric field distribution in which the angular spectrum, $\vec{\mathcal{E}}_{\tan}$, is designed by

$$\vec{\mathcal{E}}_{\tan}(k_x, k_y) = \mathcal{F}_{xy}\{\hat{z}\times(\vec{E}(\rho,\theta,z_0)\times\hat{z})\} = \mathbf{1}_{k_\rho \le \mathrm{NA}\cdot k_0}\,\hat{x}, \qquad (1)$$

where $\mathcal{F}_{xy}\{\cdot\}$ is the two-dimensional Fourier transform and $\mathbf{1}_{k_\rho \le \mathrm{NA}\cdot k_0}$ is an indicator function whose value is 1 when the tangential wavenumber $k_\rho = (k_x{}^2 + k_y{}^2)^{1/2}$ is not greater than $\mathrm{NA}\cdot k_0$, and 0 otherwise. NA is the numerical aperture of the Airy disk as defined by $\mathrm{NA} = \sin\psi$, and the radius of the EDM is set accordingly to $R = z_0 \tan\psi$. It should be noted that Eq. (1) completely determines z-component of the electric field. z-component of the electric field of x-polarized Airy disk causes anisotropic intensity distribution at $z = z_0$. There has been much research on anisotropic focal spots and beams with high-NA [30–33].

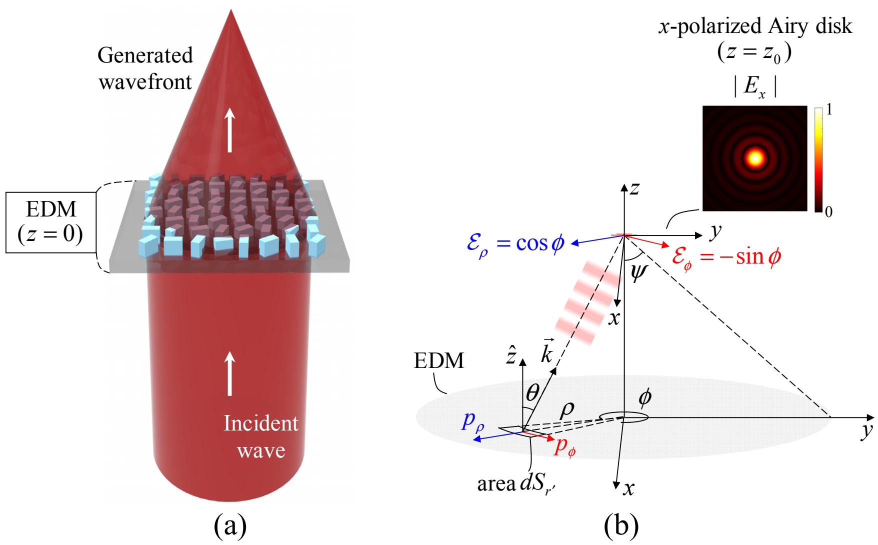

Fig. 1. (a) A schematic of an electric dipole metasurface (EDM) with subwavelength-sized dielectric rods on a flat substrate. (b) Illustration of the derivation of the electric dipole moment density of the EDM generating an x-polarized Airy disk pattern. The dipole moment densities, p_ρ and p_ϕ, in the infinitesimal area $dS_{r'}$ correspond to the angular spectral components of the x-polarized Airy disk $\mathcal{E}_\rho$ and $\mathcal{E}_\phi$ on the output plane, respectively.

In order to generate the angular spectrum components of Eq. (1) on the output plane, each electric dipole moment should be placed at the specific corresponding position on the metasurface plane, as shown in Fig. 1(b). Because the field distribution of the Airy disk is localized around $(0,0,z_0)$ and the corresponding electric dipole density varies slowly, the radiating pattern of the infinitesimal electric dipole moment, $\vec{p} = p_\rho\hat{\rho} + p_\phi\hat{\phi}$, on the EDM is the dominant contributor to the angular spectrum component, $\vec{\mathcal{E}}_{\tan} = \mathcal{E}_\rho\hat{\rho} + \mathcal{E}_\phi\hat{\phi}$, of which wavevector $\vec{k}$ should be parallel to the direction vector from the dipole to the center of the

Optics EXPRESS

Airy disk, $\vec{r}-\vec{r}'=(-\rho\cos\phi,-\rho\sin\phi,z_0)$. The radiation pattern of dipole $\vec{p}$ at position $\vec{r}'$ in infinitesimal area $dS_{r'}$ is assumed to be in the form of Green's dyadic:

$$\vec{E}=\vec{G}*\vec{p}=[1+\vec{\nabla}\vec{\nabla}]\frac{e^{-ik_0|\vec{r}-\vec{r}'|}}{4\pi\epsilon_0|\vec{r}-\vec{r}'|}\cdot\vec{p}\approx\frac{e^{-ik_0|\vec{r}-\vec{r}'|}}{4\pi\epsilon_0|\vec{r}-\vec{r}'|^3}(|\vec{r}-\vec{r}'|^2\,\vec{I}-(\vec{r}-\vec{r}')(\vec{r}-\vec{r}'))\vec{p}. \quad (2)$$

Figure 1(b) illustrates that the angular spectrum component with $\vec{k}\parallel(\vec{r}-\vec{r}')$, decomposes into TM and TE components, $\mathcal{E}_\rho$ and $\mathcal{E}_\phi$, respectively. For the *x*-polarized Airy disk, $\mathcal{E}_\rho=\cos\phi$ and $\mathcal{E}_\phi=-\sin\phi$. It should be noted that $\mathcal{E}_\rho$ is accompanied by the *z*-component of the Fourier component $-k_\rho\mathcal{E}_\rho/k_z$, while $\mathcal{E}_\phi$ is not. In turn, the generation of unit TM component needs $k_0/k_z=1/\cos\theta$ times more power than that of the unit TE component, and the in-plane components of the electric field completely determine the perpendicular component of the electric field for the unit Airy disk field. Accordingly, the dipole field on the metasurface plane decomposes into TM and TE components, p_ρ and p_ϕ, respectively, as in Fig. 1(b). Starting with Eq. (2), the electric field distribution generated by the decomposed dipole components can be represented by

$$\begin{bmatrix}E_{\mathrm{TM}}(\vec{r})\\E_{\mathrm{TE}}(\vec{r})\end{bmatrix}=\frac{1}{\epsilon_0}\frac{e^{-ik_0|\vec{r}-\vec{r}'|}}{4\pi|\vec{r}-\vec{r}'|}\begin{bmatrix}z/|\vec{r}-\vec{r}'| & 0\\0 & 1\end{bmatrix}\begin{bmatrix}p_\rho\\p_\phi\end{bmatrix}. \quad (3)$$

For fixed propagating direction $\vec{k}\parallel(\vec{r}-\vec{r}')$, the TM component of the electric dipole moment, p_ρ, radiates only the TM component with the inclination factor $z/|\vec{r}-\vec{r}'|=\cos\theta$, while p_ϕ exclusively radiates the TE component. The infinitesimal area $dS_{r'}$ corresponds to the infinitesimal area in the transverse *k*-space dS_k in the form of $|dS_{r'}/dS_k|=(\rho d\rho d\phi)/(k_\rho dk_\rho d\phi)=|\vec{r}-\vec{r}'|^4/z^2=|\vec{r}-\vec{r}'|^2/\cos^2\theta$. At the focal spot of the *x*-polarized Airy disk $\vec{r}=\vec{r}_0=z_0\hat{z}$, the electric dipole $\vec{p}=p_\rho\hat{\rho}+p_\phi\hat{\phi}$ at $\vec{r}'=\rho(\cos\phi\hat{x}+\sin\phi\hat{y})$ contributes to the Fourier components $\mathcal{E}_\rho(\vec{k})$ and $\mathcal{E}_\phi(\vec{k})$ as follows:

$$\begin{bmatrix}\mathcal{E}_\rho(\vec{k})\\\mathcal{E}_\phi(\vec{k})\end{bmatrix}\propto\left|\frac{dS_r}{dS_k}\right|\begin{bmatrix}E_{\mathrm{TM}}(\vec{r}_0)\cos\theta\\E_{\mathrm{TE}}(\vec{r}_0)\end{bmatrix}=\frac{|\vec{r}_0-\vec{r}|e^{-ik_0|\vec{r}_0-\vec{r}|}}{\epsilon_0\,4\pi}\begin{bmatrix}p_\rho\\p_\phi/\cos\theta\end{bmatrix}. \quad (4)$$

Specifically, the distribution of the electric dipoles for the generation of the *x*-polarized Airy disk described in Eq. (1) is given as:

$$\begin{bmatrix}p_\rho\\p_\phi\end{bmatrix}\propto\frac{e^{ik_0|\vec{r}_0-\vec{r}'|}}{|\vec{r}_0-\vec{r}'|}\begin{bmatrix}\mathcal{E}_\rho\\\mathcal{E}_\phi\cos^2\theta\end{bmatrix}=\frac{e^{ik_0|\vec{r}_0-\vec{r}'|}}{|\vec{r}_0-\vec{r}'|}\begin{bmatrix}\cos\phi\\-\cos^2\theta\sin\phi\end{bmatrix}\mathbf{1}_{\theta\le\psi}. \quad (5)$$

p_x and p_y are derived by applying position-dependent rotation:

$$\begin{bmatrix}p_x\\p_y\end{bmatrix}=\begin{bmatrix}\cos\phi & -\sin\phi\\\sin\phi & \cos\phi\end{bmatrix}\begin{bmatrix}p_\rho\\p_\phi\end{bmatrix}\propto\frac{e^{ik_0|\vec{r}_0-\vec{r}'|}}{|\vec{r}_0-\vec{r}'|}\begin{bmatrix}\cos^2\phi+\cos^2\theta\sin^2\phi\\\sin^2\theta\sin\phi\cos\phi\end{bmatrix}\mathbf{1}_{\theta\le\psi}. \quad (6)$$

Finally, the constructed field $\vec{E}_{\mathrm{gen}}$, via the distribution of in-plane electric dipoles in Eq. (7), can be calculated as follows:

Optics EXPRESS

$$\vec{E}_{\text{gen}}(\vec{r}) \propto \iint\limits_{x'^2+y'^2 \le z_0^2 \tan^2\psi} dx'dy' \frac{e^{-ik_0|\vec{r}-\vec{r}'|}}{|\vec{r}-\vec{r}'|^3} \frac{e^{ik_0|\vec{r}_0-\vec{r}'|}}{|\vec{r}_0-\vec{r}'|} \times$$
$$\begin{bmatrix} (r-r')^2-(x-x')^2 & -(y-y')(x-x') & -(z-z')(x-x') \\ -(x-x')(y-y') & (r-r')^2-(y-y')^2 & -(z-z')(y-y') \\ -(x-x')(z-z') & -(y-y')(z-z') & (r-r')^2-(z-z')^2 \end{bmatrix} \begin{bmatrix} \cos^2\phi+\cos^2\theta\sin^2\phi \\ \sin^2\theta\sin\phi\cos\phi \\ 0 \end{bmatrix}. \tag{7}$$

We argue that $\vec{E}_{\text{gen}} \cdot \hat{x}\big|_{z=z_0} \propto J_1(\text{NA}\cdot k_0\rho)/\rho$, that is, the x component of the generated field is the form of the Airy disk in Eq. (2). The decomposed dipole field $\vec{p}$ was normalized to produce the x-polarized Airy disk on the focal plane $z = z_0$, of the form, with precise approximation,

$$E_x = \text{NA}\cdot k_0 \frac{J_1(\text{NA}\cdot k_0\rho)}{2\pi\rho}, \tag{8}$$

where $J_1(x)$ is a first-order Bessel function of the first kind. This geometric correspondence is assisted by two previously established premises: (i) the x-polarized Airy disk is localized within the diffraction limited area, and (ii) the derived distribution of the electric dipoles varies slowly. In turn, this geometric ray-like treatment of EMD design is sufficient to generate an x-polarized Airy disk field on the output plane.

The distribution of electric dipoles of the EDM for the generation of an x-polarized Airy disk is presented in the left panel of Fig. 2. The electric dipoles are placed at the two-dimensional isotropic grid with the grid size Λ. According to the Nyquist-sampling theorem, the grid size should satisfy $\Lambda \le \lambda/2$, where λ is the wavelength of optical field. We set $\Lambda = \lambda/2$ throughout this paper. An Airy disk with any polarization is realizable at an arbitrary position via the superposition of x- and y-polarized Airy disks. As depicted in Fig. 2, the amplitude distribution of the electric field is anisotropic due to the z component of the electric field, which is required to satisfy the transversality of electromagnetic waves.

In Fig. 2, we present the amplitude distributions of the electric dipole moments for EDMs and their radiated field distributions in three dimensions. Given the focal length $z_0 = 5$ um and the numerical aperture $\text{NA} = \sin 75° = 0.966$, the E_x is almost the same as the Airy disk $2J_1(\text{NA}\cdot k_0\rho)/\rho$. Quantitatively, the quality of the constructed x-polarized Airy disk via the proposed EDM can be measured by the SNR:

$$\text{SNR} = \left[\iint |\alpha J_1(\text{NA}\cdot k_0\rho)/\rho|^2\, dxdy\right] \Big/ \left[\iint (|E_x - \alpha J_1(\text{NA}\cdot k_0\rho)/\rho|^2 + |E_y|^2) dxdy\right], \tag{9}$$

where $\alpha = \left\{\left[\iint (|E_x|^2 + |E_y|^2) dxdy\right] / \left[\iint |J_1(\text{NA}\cdot k_0\rho)/\rho|^2\, dxdy\right]\right\}^{1/2}$ normalizes the Airy disk with respect to the transverse field of the radiated field of the EDM on the focal plane. The SNR of the x-polarized Airy disk via the EDM is estimated to be 18.72. The necessity of the cross-polarized dipole component p_y can also be examined by comparing the SNR of the EDM described in Eq. (6) with that of the EDM that only has p_x. As shown in the right column of Fig. 2, the SNR of the p_y-nullified EDM is calculated to be 5.25, which is far less than that of the EDM with p_y. As seen in Fig. 2, by nullifying p_y, the amplitude distribution of E_x on the focal plane $z = z_0$ is distorted compared with that of the ideal Airy disk, and the cross-polarized component of electric field E_y clearly exists. It means that the proposed EDM described in Eq. (6) precisely generates an Airy disk. The minimizing property of the focal volume is presented in Fig. 2. From a practical viewpoint, both the *z*-directional depth resolution of the Airy focus and the transversal *x*-*y* resolution are important. The z-directional spot size in both cases is similar, at 1.276 um and 1.281 um, respectively. The miminization of the focal spot in three dimensions is achieved in the form of the Airy disk generated via the proposed EDM.

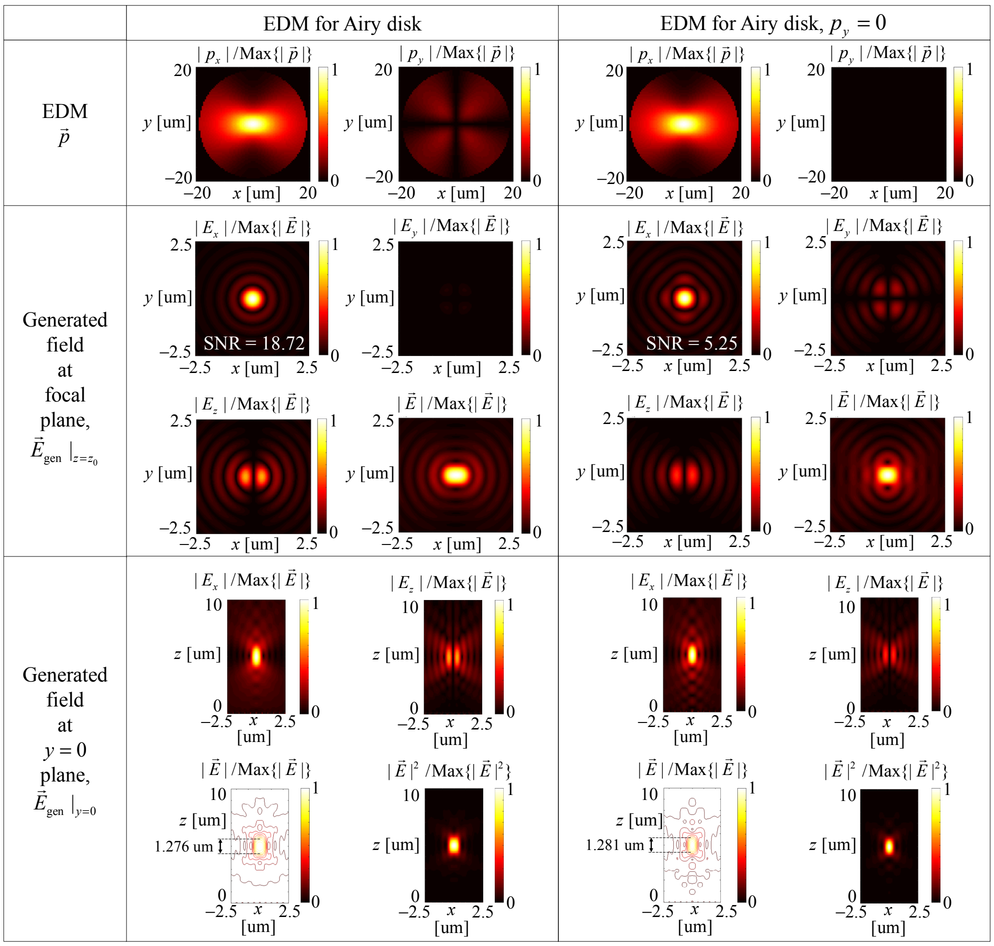

Fig. 2. Comparison between EDM distributions generating the amplitude of normalized Airy disk $2J_1(\mathrm{NA}\cdot k_0\rho)/[\mathrm{NA}\cdot k_0\rho]$, with $\mathrm{NA} = \sin(75°) = 0.966$, focal length $z_0 = 5$ um, and wavenumber $k_0 = 2\pi/(1\text{ um})$, and the reconstructed field distributions of an EDM for an *x*-polarized Airy disk (left column) and an EDM with a nullified p_y (right column). Upper row: plots of the amplitude distributions of the EDM. Middle row: generated electric field distributions on the focal plane. Lower row: electric field distributions on the $y = 0$ plane showing the focusing characteristics in three dimensions.

Based on the derived Airy disk EDM, we give an example of the generation of a Bessel-Gauss beam with a high divergence angle by decomposing it into Airy unit elements [34–39]. In the reconstruction of the Bessel-Gauss beam via an EDM, whether the EDM generates an arbitrary wavefront of spatially varying polarization, amplitude, and phase is tested.

A Bessel-Gauss beam on the focal plane is given as follows:

$$\begin{cases} E_x(\rho,\theta) = \cos(m\theta)\cdot\exp(-\rho^2/w_0{}^2)\cdot J_m(\beta\rho) \\ E_y(\rho,\theta) = \sin(m\theta)\cdot\exp(-\rho^2/w_0{}^2)\cdot J_m(\beta\rho) \end{cases}, \tag{10}$$

where m is the topological charge of the Bessel-Gauss beam, w_0 and β determine the number of rings and the size of the beam, respectively, and $J_m(x)$ is a m-th order Bessel function of the first kind [39]. Figure 3(a) displays a Bessel-Gauss beam of topological charge $m = 2$. In Fig. 3(b), the Bessel-Gauss beam is decomposed into periodically arranged linearly polarized Airy disks whose amplitudes, phases, and polarizations are obtained from the sampling process of the transverse electric field as shown in Fig. 3(a).

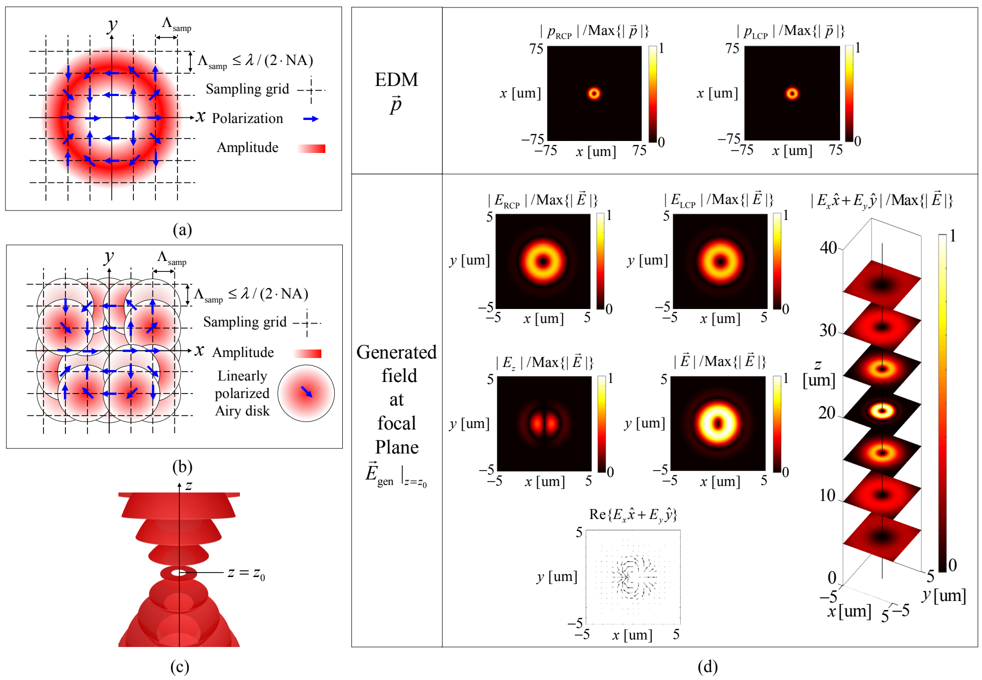

Fig. 3. Schematics for the (a) sampling and (b) reconstruction scheme for a Bessel-Gauss beam with topological charge $m = 2$. The transverse electric field on the $z = z_0$ plane is sampled at the sampling grid points, with a sampling period that satisfies the Nyquist rate of the wavefront of the beam. The transverse electric field for the Bessel-Gauss beam is always linear. The linearly polarized Airy disks, whose numerical aperture is defined by the sampling period Λ , are superposed to reconstruct the Bessel-Gauss beam. (c) Schematic of the wavefronts of the Bessel-Gauss beam. (d) Generation of the Bessel-Gauss beam via the EDM by sampling the transverse electric field on the focal plane $z = z_0 = 20$ um . The amplitude distributions of p_{RCP} and p_{LCP} of the EDM (upper row) that generate the Bessel-Gauss beam with the parameters $m = 2,\ w_0 = 2\lambda = 2$ um, and $\beta = 0.3k_0 = 1884\ \mathrm{mm}^{-1}$. Plots of the amplitude distributions of E_{RCP}, E_{LCP}, E_z, and $\vec{E}$ of the Bessel-Gauss beam on the focal plane (lower row) and the distribution of the polarization of the transverse electric field on the focal plane, and amplitude distributions of the transverse electric field at $z = 5$, 10, 15, 20, 25, 30 and 35 um (lower row).

For a given NA, the sampling grid is set to satisfy the Nyquist sampling condition $\Lambda_{\mathrm{samp}} \le \lambda/(2\cdot\mathrm{NA})$, and the highest spatial frequency $k_{\max}$ of the considered beam should

Optics EXPRESS

meet the inequality relation $k_{max} / k_0 \le \mathrm{NA}$. The later condition ensures that there is no loss of information during the reconstruction process by taking account of sufficiently high-NA.

The transverse electric field is sampled at the sampling grid points as seen in Fig. 3(a) so that the transverse electric field of the Bessel-Gauss beam on the focal plane is linearly polarized. Considering a Bessel-Gauss beam with parameters $m = 2$, $w_0 = 2\lambda$, $\beta = 0.3k_0$, and $\lambda = 1$ um, numerical testing confirms that the corresponding EDM precisely generates the target Bessel-Gauss beam in Fig. 3(d). The focal plane is placed at $z = z_0 = 20$ um, and the corresponding EDM is at $z = 0$ um. We set the numerical aperture $\mathrm{NA} = \sin 75° = 0.966$ to reconstruct all of the angular spectra of the Bessel-Gauss beam. Figure 3(d) illustrates that the EDM generates a donut-shaped, wavefront with spatially varying polarization, as depicted in Figs. 3(a) and 3(c). The peak signal-to-noise ratio (PSNR) of the reconstructed wavefront seems to be proportional to the SNR of elementary Airy disks, so to achieve a high PSNR in the reconstructed wavefront, the SNR of the elementary Airy disk needs to be high. In Fig. 4, we plot the electric field distributions of EDMs on the *xy*-plane. Figure 4 illustrates how the SNR changes when the focal length z_0 and the NA of the EDM changes. According to the numerical results, the SNR is improved by increasing z_0 and NA. For a fixed NA, a longer z_0 implies that the distribution of electric dipole moments on the EDM varies more slowly. Meanwhile, for a fixed z_0, an EDM with larger NA generates an *x*-polarized Airy disk with less distorted sidelobes, as depicted by the intensity distributions of the residual fields for the four selected EDMs on the corresponding focal plane in Fig. 4.

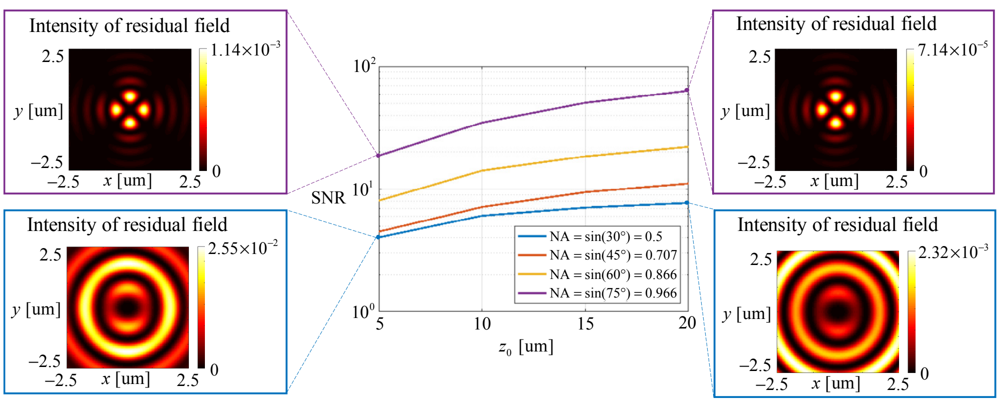

Fig. 4. $z_0 - \mathrm{SNR}$ semi-log plot (center) for various NAs and focal lengths for EDMs. Four intensity profiles (the four corners of the figure) of the residual fields, which represent the difference between E_x generated by the EDM and the Airy disk on the focal plane. The sidelobes of the Airy disk are properly reconstructed when z_0 and NA are large enough. The peak intensity of the residual field is also greatly suppressed.

3. Electric dipole metasurface for complex vector field generation

The sampling and reconstruction scheme introduced in the previous section is used to generate high quality holograms via the proposed EDM. Consider the generation of a circularly polarized hologram defined by the image in Fig. 5(a). Figure 5(b) shows that an EDM with focal length $z_0 = 5$ um and fixed $\mathrm{NA} = \sin 75° = 0.966$ produces a low-noise, right-handed circular polarization (RCP) hologram with the left-handed circular polarization (LCP) field component greatly suppressed. The peak signal-to-noise ratio (PSNR) is 76.81. To find the conditions necessary for the practical realization of ideal EDM meta-atoms, we

Optics EXPRESS

compared the quality of the reconstructed hologram from practical geometric phase metasurfaces with that of the reconstructed hologram obtained using the EDM in Fig. 5.

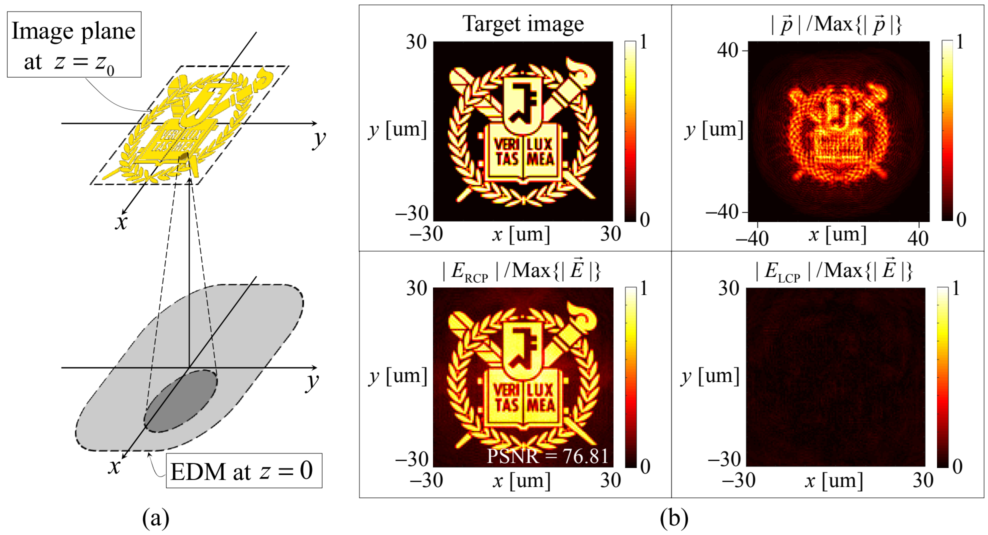

Fig. 5. (a) Schematic for hologram generation. EDM at $z = 0$ illuminated by an LCP plane wave along the + z-axis is derived by the superposition of sampled Airy disk units on the image plane $z = z_0$. (b) Plots of the target image, the electric dipole distribution of the EDM, and the corresponding field distributions on the image plane. The wavelength $\lambda = 1$ um. The PSNR is 76.81. (The trademark of Seoul National University was used with permission from Seoul National University R&DB foundation. All rights reserved, used with permission)

The electric dipole distribution for the EDM presented in Fig. 5(b) is used in the comparative test. In practice, many metasurfaces use a geometric phase scheme to generate circular-polarized spatially modulated wavefronts. Under the illumination of a circular polarized ($+\sigma$) plane wave normal to the geometric metasurface, the phase of the cross-polarized field is modulated by the geometric phase structure [1–5]. As a method to extend the phase-only modulation capability of geometric phase metasurfaces to the complex modulation of both amplitudes and phases, supercell metasurfaces have received a great deal of research attention [1, 3, 40]. Supercell structures that include a few meta-atoms are considered to be a single macro meta-molecule featuring complex amplitude modulation characteristics. Geometric phase metasurfaces (GPMs) can be categorized as EDMs. Dielectric rods with rotating angle θ act as efficient linearly polarized meta-atoms with 2θ phase modulation. We can design metasurfaces capable of complex amplitude modulation by combining two GPMs into a supercell metasurface as depicted in the left panel of Fig. 6, producing a double geometric-phase metasurface (DGPM). Given the normalized amplitude and phase modulation of $A\exp(i\phi)$, the rotation angles θ_1 and θ_2 of the two nano-rod antennas are determined by the design equation

$$\begin{cases} \theta_1 - \theta_2 = \cos^{-1}\eta A \\ \theta_1 + \theta_2 = \phi \end{cases}, \tag{11}$$

where η is a proportionality constant that controls maximum amplitude. If η is small, the two elementary antennas act as two independent phase-modulated dipoles generating a linear superposition of respective dipole fields.

Optics EXPRESS

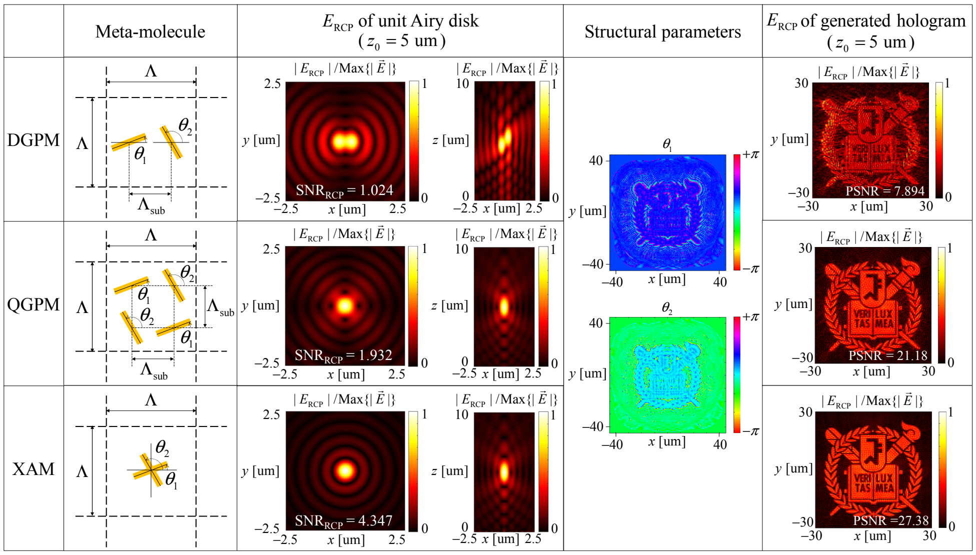

Fig. 6. Schematics of the meta-molecules for a DGPM, QGPM, and XAM (left-most panel). Amplitude distribution of the E_{RCP} for the unit RCP Airy disks via the DGPM, QGPM, and XAM on the focal plane $z = z_0 = 5$ um and on the $y = 0$ um plane (left panel). The three metasurfaces have the $\mathrm{NA} = \sin 75° = 0.966$ and the wavelength $\lambda = 1$ um. The holograms of the same target image in Fig. 5 are generated via the conventional metasurfaces DGPM, QGPM and XAM, respectively, at the focal plane $z_0 = 5$ um (right-most panel). The corresponding structural parameters θ_1 and θ_2 are presented in the third panel.

In order to enhance the SNR, we can suggest the use of quadruple geometric-phase metasurfaces (QGPMs), which combine four GPMs into one, and an X-shaped antenna metasurfaces (XAMs), which unites two elemental tilted rod antennas [40], as illustrated in the left panel of Fig. 6. DGPMs, QGPMs, and XAMs generate an RCP wavefront with a DC plane wave of opposite polarization under the illumination of an LCP plane wave on the metasurfaces. As depicted in the left panel of Fig. 6, Λ_{sub} is the distance between nearby nano-rod antennas of meta-molecules of DGPMs and QGPMs. To minimize mutual interactions of nano-rod antennas, we set $\Lambda_{\mathrm{sub}} = \Lambda / 2$. In the middle panels of Fig. 6, the local field distribution of the RCP Airy disk for the four metasurfaces around the focal spot is presented. In the far-right panel, the corresponding holographic image measured on the output plane is presented. Based on this estimation, the $\mathrm{SNR}_{\mathrm{RCP}}$ is defined as

$$\mathrm{SNR}_{\mathrm{RCP}} = \left[\iint |\alpha J_1(\mathrm{NA}\cdot k_0\rho)/\rho|^2\, dxdy\right] \Big/ \left[\iint (|E_{\mathrm{RCP}} - \alpha J_1(\mathrm{NA}\cdot k_0\rho)/\rho|^2) dxdy\right], \quad (12)$$

where $\alpha = 2\cdot \mathrm{Max}\{|E_{\mathrm{RCP}}|\}/(\mathrm{NA}\cdot k_0)$ to equalize the peak values of the calculated RCP field and the RCP Airy disk. The $\mathrm{SNR}_{\mathrm{RCP}}$ for the DGPM, QGPM, and XAM was 1.024, 1.932, and 4.347, respectively. The resultant PSNR was 7.894, 21.18, and 27.38, respectively, following the same order as the $\mathrm{SNR}_{\mathrm{RCP}}$ of the corresponding unit Airy disks. Thus, the engineering of the radiation patterns of meta-molecules is important in ensuring the quality of the hologram image. XAMs have an advantage in that they regularize the radiation pattern to be the same as that of the RCP EDM, in turn nullifying the other multipole radiation terms. It should be noted that the QGPM has a moderate $\mathrm{SNR}_{\mathrm{RCP}}$ because the magnetic dipole radiation is suppressed by the C2 symmetry of the meta-atoms in a molecule of the QGPM.

The DGPM failed to form a single focal spot, producing instead two three-dimensionally separated focal spots away from the intended position $(x, y, z) = (0, 0, 5\ \text{um})$, as seen in the middle panel of Fig. 6. In the terms of the SNR, the performance of the XAM is close to that of the EDM. It is worth mentioning that nano-rod antennas in DGPMs and QGPMs have identical shape and same frequency dispersion. These two types of metasurfaces might be used to implement dispersion engineering for broadband signal processing [41–43].

For practical applications, we discuss efficiency of the considered metasurfaces. Diffraction efficiency of meta-molecules of transmissive GPMs reaches to 1/2, assuming that low-reflection design is applied to the meta-molecules. Here, we calculate efficiency of the metasurfaces for generating a wavefront as the ratio of optical power of the generated signal to the incident power. This definition accounts for the quality of the generated wavefront as well as diffraction efficiency of meta-molecules. For example, in Fig. 6, the efficiencies of the DGPM, QGPM, and XAM are estimated to be 0.444, 0.477, and 0.236, respectively. The proportional constant η of the XAM is chosen as 0.7 which guarantees moderate interaction between arms of each meta-molecule of the XAM. GPMs for generating such large bandwidth holograms suffer from low efficiency, due to their low PSNR.

The comparative study of the DGPM, the QGPM, and the XAM indicates that the radiation patterns of the meta-molecules are crucial to the generation of extremely high SNRs for high-NA focal spots. These conventional metasurfaces are only capable of generating wavefronts with a fixed circular polarization. The spatial multiplexing of two DGPMs, QGPMs, or XAMs with polarization filtering might generate true EDM meta-atoms for complete vector field generation. The irregular radiation patterns of meta-molecules ascribed to macro-pixel integration can lead to metasurfaces with low SNRs, but the regularization of meta-atoms requires further research.

4. Conclusion

In this study, we have investigated Huygens' optical vector wave field synthesis scheme and considered an EDM with full freedom in terms of amplitude, phase, and polarization as the ultimate form of optical field modulation metasurface. Meta-atom structures with a full degree of freedom have not previously been proposed but here we describe an EDM distribution design and the practical design issues facing vector field synthesis in the deep-subwavelength multiplexing of XAM or QGPM structures that afford polarization control and complex modulation. The described scheme paves the way for future practical metasurface applications that require the capabilities of precise generation of optical field with large bandwidth.

Funding

National Research Foundation of Korea (NRF); Ministry of Science, ICT and Future Planning (MSIP) (NRF-2017R1A2B2006676).